Stanford Exploration Project, Report 120, May 3, 2005, pages 257–272

ADCIGs for forward-scattered wavefields

Jeff Shragge, Brad Artman, and Biondo Biondi[1]

ABSTRACT

We extend the 2-D theory of angle-domain common-image gathers (ADCIGs) to forward-scattered wavefields, and present a method for extracting reflectivity as a function of either the reflected or converted-wave receiver-side scattering angle. We use the shot-profile configuration of wave-equation migration along with planar source and receiver wavefields to generate an analytic hyper-plane surface in the intermediate offset-domain common-image gather space. Geometrical relations and partial derivatives of the hyper-plane function generate six constraint equations for the the unknown six parameters, allowing us to solve for the source- and receiver-side reflection angles and geologic dip angle. Results of numerical experiments indicate that information on wavefield focusing is present in forward-scattered ADCIGs, which suggests that this algorithm may be useful tool for improving wave-equation based tomography of transmission wavefields.

INTRODUCTION

Conventional seismic exploration surveys acquire P-wave reflection data with surface-based acquisition geometry. Increasingly, though, non-conventional surveys provide additional and complementary constraints on the seismic imaging process. One non-conventional survey example is massive 3-D vertical seismic profiling (VSP), which generates increased subsurface ray coverage and affords enhanced resolution of complex geologic structure (Payne et al., 1994; Bicquart, 1998; Sullivan et al., 2003). A second example is the use of long-offset refracted waves in conventional reflection surveys to improve migration velocity analysis (MVA) through wavefield inversion (Pratt, 1999; Sirgue and Pratt, 2004). Non-conventional surveys often incorporate alternative acquisition geometry and/or novel sources such as in passive seismic imaging; many are designed to measure forward-scattered energy with sufficient spatial sampling to permit wavefield-based processing. Hence, a careful examination the utility of forward-scattered wavefields in the seismic imaging process is warranted.

The forward-scattering scenario arises when a source wavefield interacts with discontinuous structure generating a secondary scattered wavefield of diffracted and converted energy that propagates sub-parallel to the source wavefield. Importantly, because these two wavefields travel in similar directions, and thereby sample the subsurface in a similar way, they contain important velocity profile information in both absolute (i.e., direct waves) and relative (i.e., differential) travel-times. The utility of this information for velocity analysis and/or

[1]**email:** jeff@sep.stanford.edu, brad@sep.stanford.edu, biondo@sep.stanford.edu

imaging is well-known, and is used frequently in many branches of seismology (Langston, 1977; VanDecar, 1991; Bostock et al., 2001; Sheley and Schuster, 2003).

Most forward-scattering MVA and imaging methods do not process entire wavefield records, and instead rely on the analysis of picked relative or global traveltimes. Analogous to conventional reflection seismic processing, though, significant MVA and imaging improvements should be achievable by moving from forward-scattered traveltime-based processing to forward-scattered wavefield inversion methods. However, before we can test this assertion, a number of forward-scattering MVA and imaging tools must be developed - in particular, the forward-scattering equivalent of the angle domain common image gather (ADCIG) (Prucha et al., 1999; Sava and Fomel, 2003a; Biondi, 2005; Rosales and Biondi, 2005)

In this paper, we modify existing 2-D ADCIG theory to account for the differences arising in the forward-scattering scenario. We use the shot-profile configuration of wave-equation migration to provide a ADCIG framework for both forward-scattered diffracted ($P-P$) and converted ($P-S$) wavefields. We begin by reviewing the wavefield extrapolation and imaging condition steps of shot-profile migration. We then specify planar source and receiver wavefields, and generate parametric surfaces in the intermediate offset-domain common-image gather (ODCIG) space. Subsequently, we show how to transform ODCIGs to their angle domain representation, and detail how to compute angle-dependent source- and receiver-side reflectivity and the geologic dip angle directly from the ODCIG volume. We then apply the approach to a synthetic teleseismic plane-wave data set (Shragge, 2003). This data set is comprised of elastic wavefields, which allows us to test our ADCIG theory for both $P-P$ and $P-S$ forward-scattered scenarios.

SHOT-PROFILE MIGRATION

Shot-profile migration reconstructs the subsurface reflectivity profile by approximately reconstructing the physics of wave-propagation and scattering that generated individual shot records. Central to this formulation is the notion of two independent wavefields: a source wavefield, S, that interacts with discontinuous structure to generate a scattered receiver wavefield, R. The shot-profile migration algorithm consists of two processing steps. The first step is the independent propagation of the S and R wavefields. The second step combines wavefields S and R in a physical imaging condition to generate a map of subsurface reflectivity.

The first shot-profile migration step is an independent extrapolation of S and R, which requires the recursive solution of (Claerbout, 1985),

$$\begin{aligned} S(x_s, z_s + \Delta z_s; \omega) = &\quad S(x_s, z_s; \omega)\, \mathrm{e}^{\pm \mathrm{i} k_{z_s} \Delta z_s}, \\ R(x_r, z_r + \Delta z_r; \omega) = &\quad R(x_r, z_r; \omega)\, \mathrm{e}^{-\mathrm{i} k_{z_r} \Delta z_r}, \end{aligned} \tag{1}$$

where k_{z_s} and k_{z_r} are the source and receiver vertical wavenumbers from the wave-equation dispersion relationship, Δz_s and Δz_r are depth step intervals, and ω is angular frequency. Successive applications of the complex exponential operators in Equation (1) generate the full S and R wavefield volumes, $S(\mathbf{x_s}; \omega)$ and $R(\mathbf{x_r}; \omega)$, at all source, $\mathbf{x_s}$, and receiver, $\mathbf{x_r}$, points in model space.

The source wavefield extrapolation operator in Equation (1) includes symbol $\pm$ to distinguish between forward- and backscattering migration scenarios. This parameter explains the causality arguments illustrated in Figure 1. The four panels represent the forward (i.e., modeling) and adjoint (i.e., migration) propagation of wavefields for both the forward- and backscattered scenarios. Causal propagation is indicated with a forward time-arrow and a positive sign in the extrapolation operator.

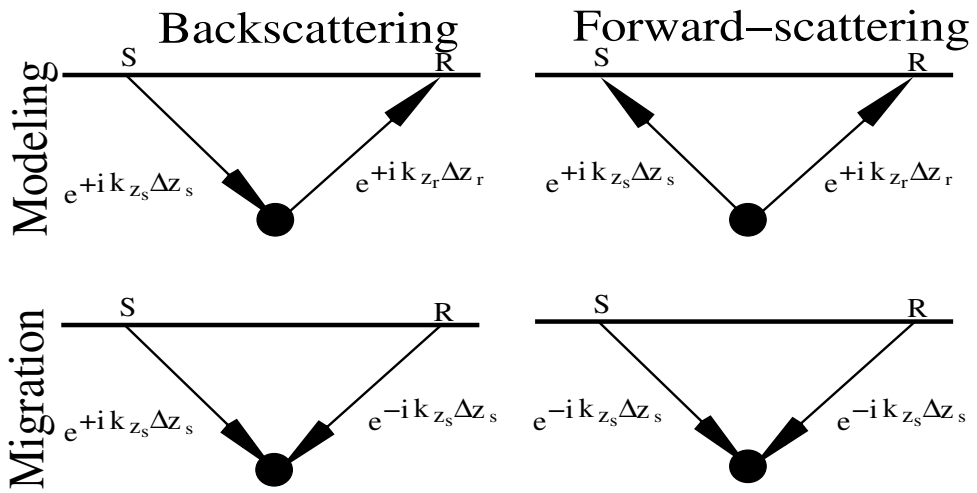

Figure 1: Sketch representing causality arguments for forward- and backscattering scenarios. Time-arrows and positive extrapolation operators indicate causal propagation. Upper left: Backscattered modeling; lower left: backscattered migration; upper right: forward-scattered modeling; and lower right: forward-scattered migration. Note the differing extrapolation operators required for migration that arise from causality arguments. jeff2-FSBS [NR]

In backscattered modeling (upper left), a surface-excited source wavefield propagates to a point scatterer and then diffracts as a scattered wavefield, R, upward to the surface. Migrating backscattered wavefields (lower left) propagates R backward in time into the subsurface, which requires reversing the direction of the receiver time arrow and the sign of the receiver extrapolation operator. In forward-scattered modeling (upper right), an upgoing source wavefield impinging from below interacts with the point scatterer, again generating an upgoing scattered wavefield, R. Migrating forward-scattered waves (lower right) requires propagating both S and R backward in time into the subsurface, which reverses the direction of the two time arrows and the signs of both extrapolation operators.

The second shot-profile migration step generates an image, I, of subsurface reflectivity through an evaluation of a physical imaging condition (Claerbout, 1971). The most basic imaging condition extracts the zero-lag coefficient of the correlation of wavefields S and R. An important extension includes an additional image-space dimension, subsurface half-offset **h**, generated by shifting S and R in opposing directions by distance **h** prior to correlation (Rickett and Sava, 2002). We emphasize that **h** is not equivalent to the surface offset parameters often encountered in shot-geophone or Kirchhoff migration approaches. We write this step with the

following equation,

$$I(\mathbf{x},\mathbf{h}) = \sum_{\omega} [\delta(\mathbf{x_s} - \mathbf{x} - \mathbf{h}) * S(\mathbf{x_s};\omega)] \left[\overline{R(\mathbf{x_r};\omega)} * \delta(\mathbf{x_r} - \mathbf{x} + \mathbf{h})\right], \tag{2}$$

where $\mathbf{x}$ is the spatial variable of image-space, $\overline{R}$ is the complex conjugate of R, and $*$ indicates convolution. The resulting image volume is termed an offset-domain common-image gather (ODCIG). In general, the shifting operation can be oriented in any direction; however, generating a complete 2-D ODCIG volume requires shifts in only two orthogonal directions. For computational simplicity, this is usually done along the horizontal (HODCIGs) and vertical (VODCIGs) axes (Biondi and Symes, 2004).

PLANE-WAVE ODCIGS

In this section, we examine the ODCIG volumes generated by forward-scattered wavefields. For simplicity, we illustrate these concepts using plane-wave S and R wavefields. We also assume that S and R propagate at constant, though not necessarily equal, slownesses (i.e., reciprocal of velocity). These idealizations allow us to generate an analytic surface in ODCIG space for both $P-P$ diffracted and $P-S$ converted waves. We specify planar S and R wavefields in constant velocity media using source and receiver ray parameter vectors, $\mathbf{w}_s$ and $\mathbf{w}_r$, defined by,

$$\mathbf{w}_s = \left[p_s, q_s\right] = s_s \ [\sin\beta_s, \cos\beta_s] \quad \text{and} \quad \mathbf{w}_r = \left[p_r, q_r\right] = s_r \ [\sin\beta_r, \cos\beta_r], \tag{3}$$

where p_s and p_r are the source and receiver horizontal ray parameters, q_s and q_r are the source and receiver vertical ray parameters, and s_s and s_r are the source and receiver wavefield propagation slownesses, respectively. Also, we use a convention where angles are defined clockwise positive with respect to the vertical depth axis.

Forward-scattered S and R wavefields must satisfy the causality arguments illustrated in Figure 1, which requires a negative sign in the source and receiver extrapolation operators. Using the aforementioned assumptions, we generate the following extrapolated S and R wavefield volumes,

$$S(\mathbf{x_s};t) = \delta(t + \mathbf{w}_s \cdot \mathbf{x_s}) \quad \text{and} \quad R(\mathbf{x_r};t) = \delta(t + \mathbf{w}_r \cdot \mathbf{x_r}). \tag{4}$$

Applying a Fourier transform over the t-axis of both S and R yields,

$$S(\mathbf{x_s};\omega) = \exp(-i\omega\mathbf{w}_s \cdot \mathbf{x_s}) \quad \text{and} \quad R(\mathbf{x_r};\omega) = \exp(-i\omega\mathbf{w}_r \cdot \mathbf{x_r}). \tag{5}$$

Evaluating the imaging condition in Equation (2) with the wavefields in Equation (5) generates the following image-space volume,

$$\begin{aligned} I(\mathbf{x},\mathbf{h}) = &\ \textstyle\sum_\omega \delta(\mathbf{x_s} - \mathbf{x} - \mathbf{h}) * \exp(-i\omega\mathbf{w}_s \cdot \mathbf{x_s}) \left[\overline{\exp(-i\omega\mathbf{w}_r \cdot \mathbf{x_r})} * \delta(\mathbf{x_r} - \mathbf{x} + \mathbf{h})\right], \\ = &\ \textstyle\sum_\omega \exp(-i\omega[\mathbf{x} \cdot (\mathbf{w}_s - \mathbf{w}_r) + \mathbf{h} \cdot (\mathbf{w}_s + \mathbf{w}_r)]). \\ = &\ \delta[\mathbf{x} \cdot (\mathbf{w}_s - \mathbf{w}_r) + \mathbf{h} \cdot (\mathbf{w}_s + \mathbf{w}_r)]. \end{aligned} \tag{6}$$

The non-zero δ-function argument,

$$x\,(p_r - p_s) + z\,(q_r - q_s) - h_x\,(p_r + p_s) - h_z\,(q_r + q_s) = 0, \tag{7}$$

represents an analytic forward-scattered ODCIG hyper-plane surface. Importantly, this surface interrelates source and receiver plane-wave angles, propagation slownesses and image-space variables, **x** and **h**. In the next section, we manipulate this formula to generate constraint equations that help isolate the receiver-side contribution to the total reflection angle.

FROM ODCIGS TO ADCIGS

An ODCIG can be transformed to another image-space volume, termed an angle-domain common-image gather (ADCIG), representing reflectivity as a function of reflection angle. Sava and Fomel (2003b) present a post-imaging, Fourier-domain transform between these spaces appropriate for conventional reflection wavefields. However, as discussed by Rosales and Rickett (2001), this transform does not hold for converted waves because Snell's Law partitions the total reflection angle into unequal source- and receiver-side reflection contributions.

Figure 2 illustrates the generalized geometry of the forward-scattering scenario for a subsurface geologic discontinuity, $\overline{\mathbf{I}}$, oriented at geologic dip angle, α, with normal, $\overline{\mathbf{n}}$. An upgoing planar source wavefield propagating at angle β_s to the upward vertical has already interacted at $\overline{\mathbf{I}}$ to generate an upgoing, planar wavefield propagating at angle β_r. For $P-P$ interactions, Snell's Law requires that total reflection opening angle, 2γ, is split equally between the source- and receiver-side reflection angles (i.e., $\gamma = \gamma_r = \gamma_s$). For $P-S$ conversions, Snell's Law requires that angle 2γ is not bisected into equal components, leaving γ_s unequal to γ_r. Hence, additional constraint equations must be included to isolate the receiver-side reflectivity contributions.

Generating Constraint Equations

Generating ADCIGs for forward-scattered wavefields requires specifying reflectivity as a function of either the source-side, γ_s, or receiver-side, γ_r, reflection angles. Either choice, though, requires isolating one angle from a system with 6 free parameters: $\beta_s, \beta_r, \gamma_s, \gamma_r, \alpha$, and γ. Hence, solving for, say, γ_r requires specifying 6 constraint equations.

Three constraint equations are specified by geometric relationships (c.f. Figure 2). The first constraint equation is a local conservation of reflection angle given by,

$$2\gamma = \gamma_s + \gamma_r. \tag{8}$$

The second and third constraint equations derive from a global conservation of reflection angle arguments that relate the S and R plane-wave angles, geologic dip, and the source- and receiver-side reflection angles through (Biondi, 2005),

$$\beta_s = \alpha - \gamma = \alpha - \frac{\gamma_s + \gamma_r}{2}, \tag{9}$$

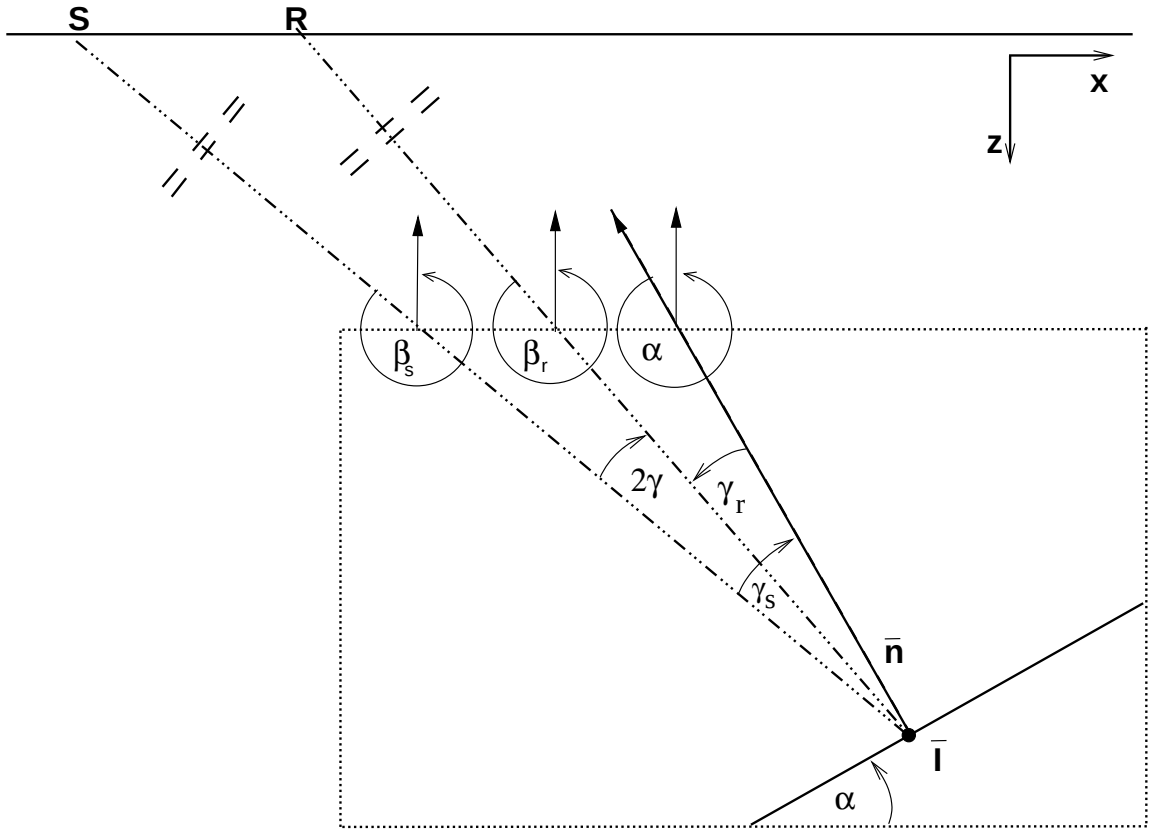

Figure 2: Sketch denoting the forward-scattered converted wave scenario. An upgoing planar source wavefield propagating at angle β_s has already interacted with surface $\bar{\mathbf{I}}$ to generate an upgoing planar scattered wavefield, R, propagating at angle β_r. The total reflection angle, 2γ, is partitioned into source- and receiver-side reflection angles, γ_s and γ_r, according to Snell's Law. Arrows are included on angles to show the sense of rotation, where (counter)clockwise angles are taken here to be (negative) positive quantities. jeff2-cig-simple-v4 [NR]

and,

$$\beta_r = \alpha + \gamma = \alpha + \frac{\gamma_s + \gamma_r}{2}. \tag{10}$$

Snell's Law provides a fourth physical constraint equation by relating the source- and receiver-side reflection angles with the local propagation slownesses,

$$s_s \sin\gamma_s = s_r \sin\gamma_r, \tag{11}$$

which can be rewritten using Equation (10) as,

$$\tan\gamma_r = \frac{\sin 2\gamma}{\frac{s_r}{s_s} + \cos 2\gamma}. \tag{12}$$

Constraint equations (8-11) do not incorporate physical observables measured from the generated image volume. However, we can calculate image-space dips in both the horizontal subsurface half-offset, $\frac{\partial z}{\partial h_x}$, and midpoint, $\frac{\partial z}{\partial x}$, directions. Thus, the final two constraint equations relating measured dips to free parameters can be obtained by taking the appropriate partial derivatives of the parametric hyper-plane surface in Equation (7),

$$\left.\frac{\partial z}{\partial h_x}\right|_{x,h_z} = \frac{p_r + p_s}{q_r - q_s} = \frac{s_r \sin(\alpha+\gamma) - s_s \sin(\alpha-\gamma)}{s_r \cos(\alpha+\gamma) + s_s \cos(\alpha-\gamma)}, \tag{13}$$

and

$$\left.\frac{\partial z}{\partial x}\right|_{z,h_z} = -\frac{p_r + p_s}{q_r + q_s} = -\frac{s_r \sin(\alpha+\gamma) + s_s \sin(\alpha-\gamma)}{s_r \cos(\alpha+\gamma) + s_s \cos(\alpha-\gamma)}. \tag{14}$$

We rewrite Equations (13) and (14) using the trigonometric angle addition and subtraction rules,

$$\left.\frac{\partial z}{\partial h_x}\right|_{x,h_z} = \frac{(s_r - s_s)\cos\alpha \sin\gamma + (s_r + s_s)\sin\alpha\cos\gamma}{(s_r - s_s)\cos\alpha\cos\gamma + (s_r + s_s)\sin\alpha\sin\gamma}, \tag{15}$$

and,

$$\left.\frac{\partial z}{\partial x}\right|_{z,h_z} = -\frac{(s_r + s_s)\cos\alpha \sin\gamma + (s_r - s_s)\sin\alpha\cos\gamma}{(s_r - s_s)\cos\alpha\cos\gamma - (s_r + s_s)\sin\alpha\sin\gamma}, \tag{16}$$

which we rearrange to yield,

$$\left.\frac{\partial z}{\partial h_x}\right|_{x,h_z} = \frac{\phi\tan\gamma + \tan\alpha}{\phi - \tan\alpha\tan\gamma} \quad \text{and} \quad \left.\frac{\partial z}{\partial x}\right|_{z,h_z} = -\frac{\tan\gamma + \phi\tan\alpha}{\phi - \tan\alpha\tan\gamma}, \tag{17}$$

where ϕ is a "normalized difference" of slownesses given by, $\phi = \frac{s_r - s_s}{s_r + s_s}$. Solving for $\tan\gamma$ and $\tan\alpha$ leads to,

$$\tan\gamma = \frac{\phi\,\frac{\partial z}{\partial h_x} - \tan\alpha}{\phi + \frac{\partial z}{\partial h_x}\tan\alpha} \quad \text{and} \quad \tan\alpha = \frac{\tan\gamma + \phi\,\frac{\partial z}{\partial x}}{\frac{\partial z}{\partial x}\tan\gamma - \phi}, \tag{18}$$

where the parameters held constant during partial differentiation are no longer explicitly written. These two expressions can be manipulated to specify independent equations for reflection angle, γ,

$$\tan^2\gamma\left[\phi\frac{\partial z}{\partial x}+\frac{\partial z}{\partial h_x}\right]+\tan\gamma\left[1-\phi^2\right]+\phi\left[\phi\frac{\partial z}{\partial h_x}+\frac{\partial z}{\partial x}\right]=0, \tag{19}$$

and true geologic dip, α,

$$\tan^2\alpha\left[\phi\frac{\partial z}{\partial h_x}-\frac{\partial z}{\partial x}\right]+\tan\alpha\left[1+\phi^2\right]+\phi\left[\phi\frac{\partial z}{\partial x}+\frac{\partial z}{\partial h_x}\right]=0. \tag{20}$$

When source and receiver propagation slownesses are equal (i.e., $\phi=0$), these quadratic equations reduce to,

$$\frac{\partial z}{\partial h_x}=-\cot\gamma \quad \text{and} \quad \frac{\partial z}{\partial x}=-\cot\alpha. \tag{21}$$

which is similar to the expressions derived for the backscattered case save for a $\pi/2$ phase rotation (i.e., $\tan x=\cot(\pi/2-x)$). Finally, the solution for the receiver-side reflection angle, γ_r, is obtained from angle γ through the relation specified in Equation (12).

In Equations (13) and (14), we differentiated with respect to variables, x and h_x. This choice was one step in the development of horizontal ADCIGs. Equally, we can create vertical ADCIGs by developing two constraint equations from partial derivatives with respect to vertical variables, z and h_z, holding horizontal variables x and h_x constant. Vertical ADCIGs are then generated through introduction of these functions into Equations (15-20). Biondi and Symes (2004) detail situations where it is more advantageous to use vertical ADCIGs than their horizontal counterparts. In particular, vertical ADCIGs provide better spatial resolution for scenarios where the wavefield propagation direction is oriented at steep angles to the geologic dip-field.

NUMERICAL EXAMPLES

In this section, we present numerical tests of the theory developed above. We provide the proof-of-concept using a plane-wave teleseismic data set (Shragge, 2003). This data set is comprised of elastic wavefields, which allows us to test both the diffracted and converted scattering scenarios. The idealized model, shown in Figure 3, is comprised of three materials with differing elastic properties. A low-velocity crustal layer (white) overlies a faster upper mantle (dark gray). At the location of the suture, crustal material from the lithospheric block to the left bifurcates, with the lower segment descending into the mantle. At the depth of approximately 40 km, the relict (black) converts to velocities and density higher than the surrounding mantle (with a proportionally greater increase in shear-wave velocity) and thereafter folds and thins to the right of the model. Structural dips in the model are generally quite low (i.e., less than 20°); however, sub-vertical discontinuities are present in the zone of short-wavelength structure between x=120 and x=160.

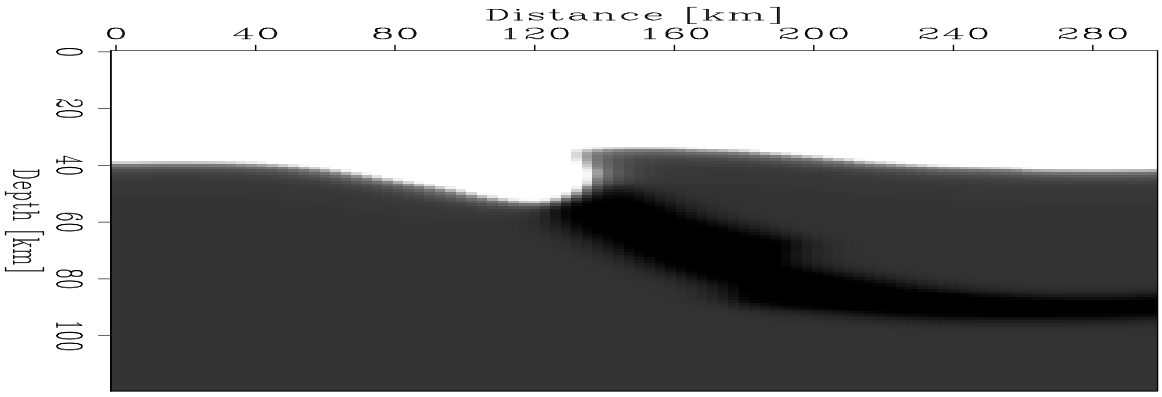

Figure 3: Smoothed version of structural model used in test. jeff2-Vel [ER]

Several sets of two-component seismograms were computed through this model using a 2-D, elastic pseudo-spectral finite-difference code (Kosloff et al., 1990). The seismograms comprise a suite of plane P-wave sources interacting with the model over a range of incident horizontal slownesses, $p_s = [\pm 0.05, \pm 0.06, \pm 0.07]\text{skm}^{-1}$. We rotated the output data from the computational orientation (i.e., $\mathbf{U} = [U_1, U_3]$) to a wave-vector orientation (i.e., $\mathbf{w} = [P, SV]$) via the free-surface transfer matrix (Kennett, 1991).

Figure 4 presents examples of P-wave (top panels) and S-wave (bottom panels) data sections. The left and right panels show data for plane-wave sources incident from the left and right sides of the model in Figure 3, respectively. We are interested in imaging are the $P-P$ diffracted waves from the zone of short wavelength structure immediately following the plane-wave arrival, and the $P-S$ diffracted and converted waves arriving shortly thereafter.

This vector-wavefield processing yields P- and S-wave data sections appropriate for use in shot-profile migration (Shragge et al., 2005). We migrated the data sections for both $P-P$ and $P-S$ scattering modes. We present the image volumes in Figures 5 and 6, where horizontal and vertical ADCIGs are shown in the upper and lower panels, respectively. The upper panel of Figure 5 shows a vertical streak around 130 km in midpoint. This indicates that because of the low geologic dip angles in this model, horizontal ADCIGs computed from forward-scattered $P-P$ migrations afford low resolution of the imaged structure, and are not likely to be useful either for MVA or imaging.

In addition, we computed vertical ADCIGs using the method described in the above section (i.e., by replacing horizontal variables x and h_x with vertical variables z and h_z). The vertical ADCIG shown in the lower panels have a slightly better spatial localization of energy. Note that migrated energy in panel d) focuses about 90°, which is the forward-scattered equivalent of a zero-offset reflection. Also imaged is a cross-hair pattern about the target zone in panel c) that is directly analogous to smearing commonly observed in tomographic images that derives from limited ray coverage.

The migration results for forward-scattered $P-S$ conversions are shown in Figure 6. However, we have not yet fully implemented Equation (19), and use Equation (21) as a proxy

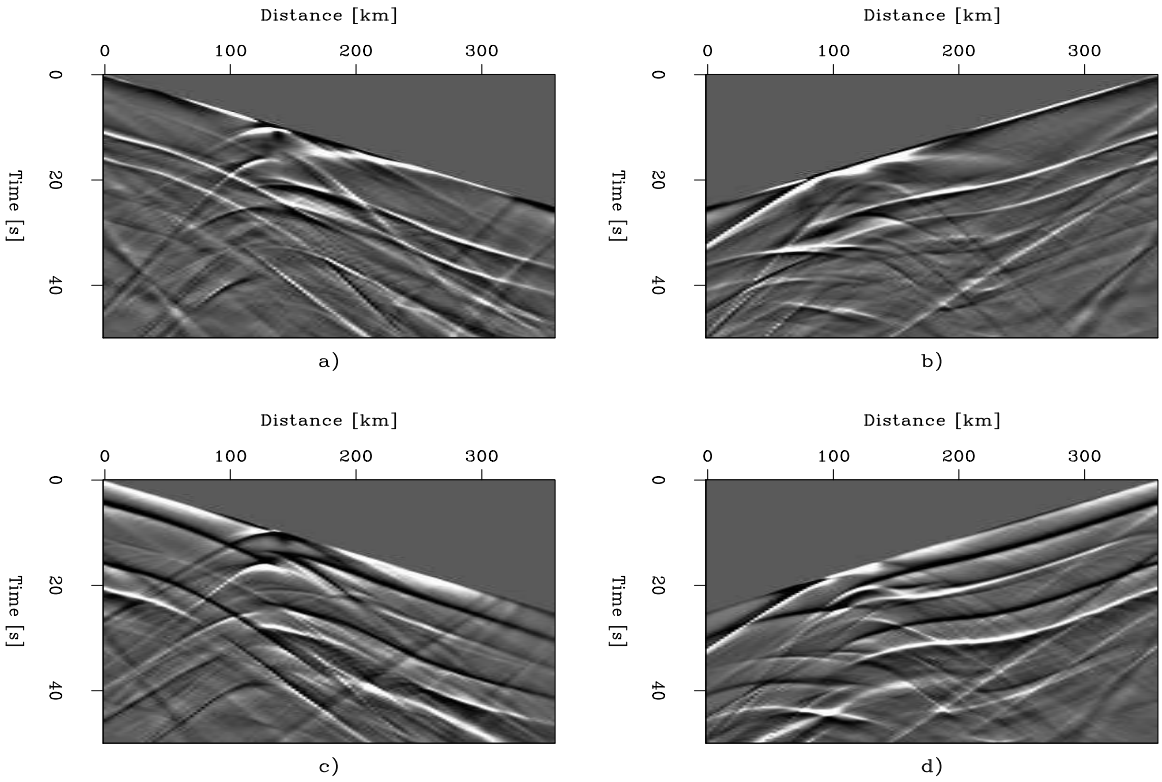

Figure 4: Examples of plane-wave data used in migration and ADCIG test. a) left-incident P-wave; b) right-incident P-wave; c) left-incident S-wave; and d) right-incident S-wave. jeff2-data [ER]

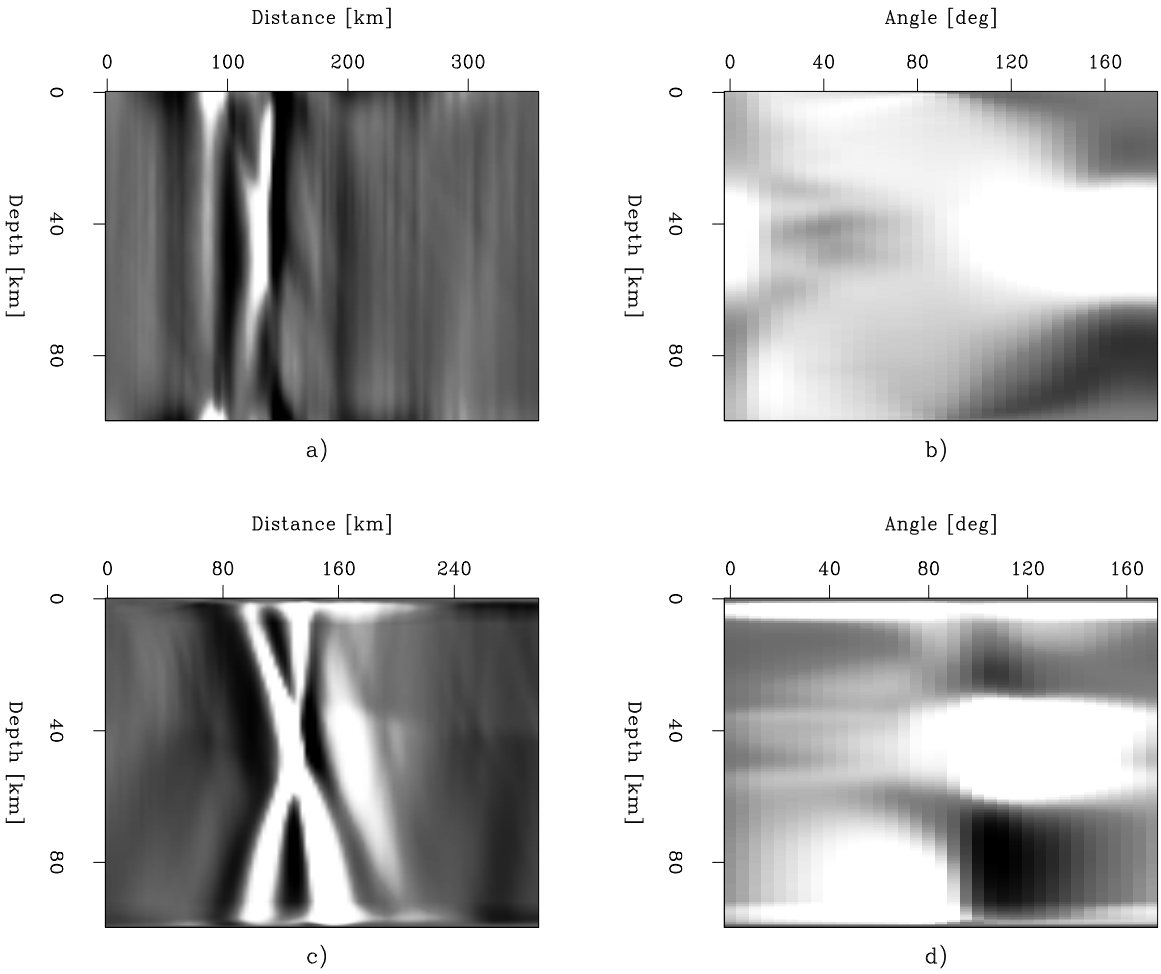

Figure 5: ADCIGs for forward-scattered $P-P$ diffracted wavefields. a) slice through horizontal ADCIG volume at angle 150°; b) slice through horizontal ADCIG volume at x=126 km; c) slice through vertical ADCIG at angle 110°; and d) slice through vertical ADCIG at x=126 km. Note that the vertical ADCIGs has a slightly better spatial localization of energy. jeff2-Q1 [CR]

instead. This is not too grievous of an approximation, as shown by Rosales and Biondi (2005). Hence, angles are not exactly in the correct position. Future work will implement the appropriate expressions. The upper panels show the $P-S$ horizontal ADCIG. Panel b) exhibits clusters of energy on both sides of the 90° mark. These represent groups of 3 plane-waves impinging from the right and left sides of the model that are mapped to different sides of the 90° normal axis. Relative to the equivalent panels in Figure 5, the forward-scattered horizontal ADCIG indicates that forward-scattered converted waves afford significantly higher resolution than $P-P$ diffractions. This observation is a consequence of the direct link between increased differential arrival times and improved spatial resolution. The vertical ADCIG volume, shown in the lower panels, again affords better resolution of sub-vertical structure than sub-horizontal interfaces. The zone of short-wavelength structure is better imaged than its counterpart in Figure 5, and has better angle-domain localization.

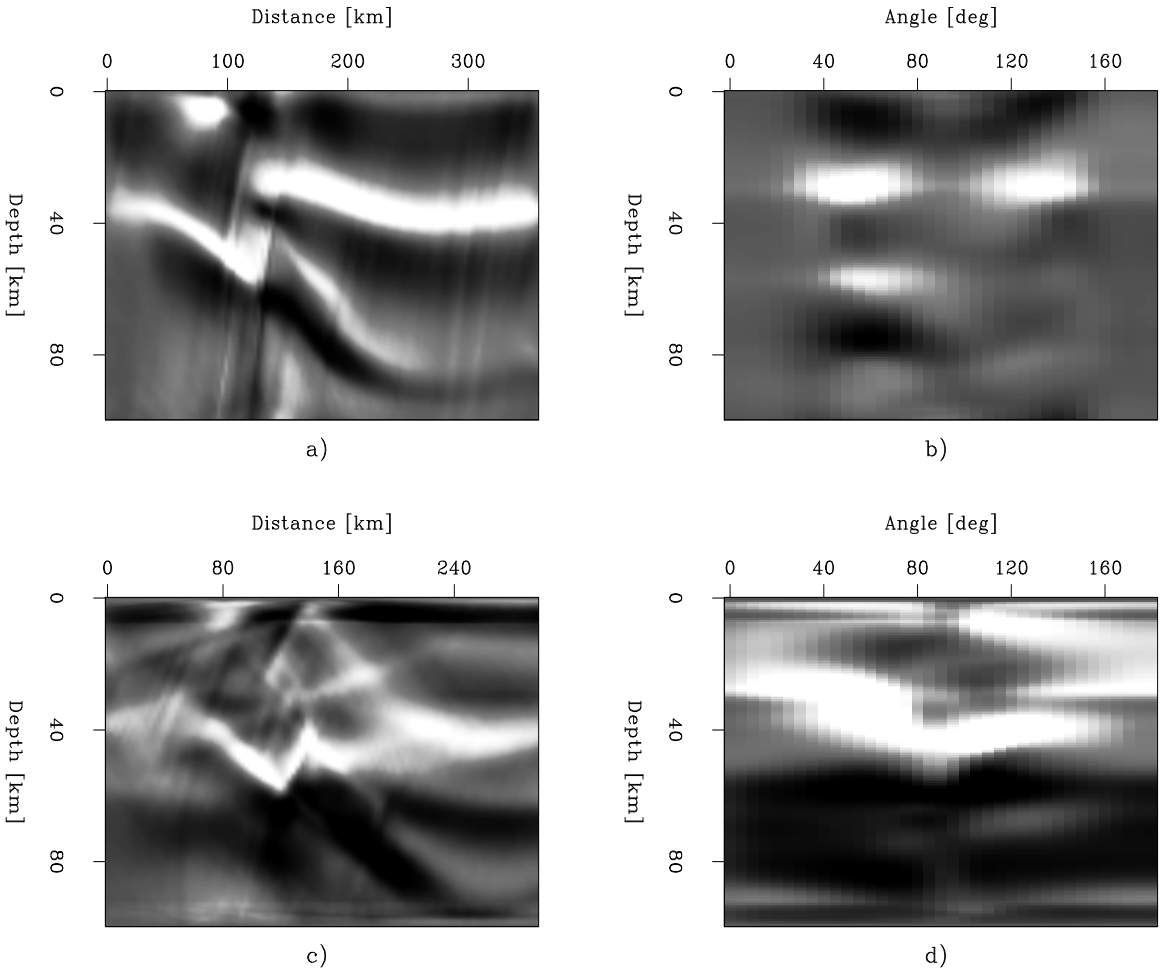

Figure 6: ADCIGs for forward-scattered $P-S$ converted wavefields. a) slice through horizontal ADCIG volume at angle 55°; b) slice through horizontal ADCIG volume at x=174 km; c) slice through vertical ADCIG at angle 90°; and d) slice through vertical ADCIG at x=138 km. jeff2-Q2 [CR]

DISCUSSION AND FUTURE WORK

The numerical tests illustrate that forward-scattered wavefield imaging can lead to interpretable ADCIG volumes. In particular, we show that vertical ADCIGs are able to resolve geologic dips oriented sub-parallel to the plane-wave propagation direction. Conversely, horizontal ADCIGs are shown to afford little resolution to flat-lying reflectors. This data set, though, does not provide an ideal test of the forward-scattered imaging approach. The shots are both limited in number and distribution of wavenumbers within each shot-record. Higher frequency content of the data is required before the spatial resolution of forward-scattered ADCIGs is fully assessed. In the future, we will apply the methodology to data sets containing forward-scattered waves, potentially including cross-hole seismic, VSP, and long-offset surface reflection data.

CONCLUDING REMARKS

We extend the 2-D ADCIG theory to include forward-scattered wavefields comprised of $P-P$ diffracted and $P-S$ scattering. We develop a series of six equations for the six unknown parameters, which allows us to estimate either the source- or receiver-side, angle-dependent reflectivity directly from ODCIGs volumes. Numerical tests illustrate forward-scattered wavefields are useful for imaging. This observation motivates further testing of the developed algorithms on field data scenarios, including cross-hole seismic, VSP, and long-offset reflection data. Results of numerical experiments indicate that information on wavefield focusing is present in forward-scattered ADCIGs, which suggests that this algorithm may be useful tool for improving wave-equation based tomography of transmission wavefields.

ACKNOWLEDGMENTS

We would like to thank Charlie Wilson for helpful discussions early on in the development.

REFERENCES

Bicquart, P., 1998, Application of Kirchhoff depth migration to 3D VSP: 68th Ann. Internat. Mtg., Soc. of Expl. Geophys., Expanded Abstracts, 389–392.

Biondi, B., and Symes, W., 2004, Angle-domain common-image gathers for migration velocity analysis by wavefield-continuation imaging: Geophysics, **69**, 1283–1298.

Biondi, B., 2005, Angle-domain common image gathers for anisotropic migration: SEP–**120**, 77–104.

Bostock, M., Rondenay, S., and Shragge, J., 2001, Multi-parameter two-dimensional inversion of scattered teleseismic body waves, 1. Theory for oblique incidence: J. Geophys. Res., **106**, 30771–30782.

Claerbout, J., 1971, Toward a unified theory of reflector mapping: Geophysics, **36**, 467–481.

Claerbout, J., 1985, Imaging the Earth's Interior: Stanford University.

Kennett, B., 1991, The removal of free surface interactions from three-component seismograms: J. Geophys. Res., **104**, 153–163.

Kosloff, D., Kessler, D., Filho, A., Tessmer, E., Behle, A., and Strahilevitz, R., 1990, Solution of the equations of dynamic elasticity by a Chebychev spectral method: Geophysics, **55**, 734–748.

Langston, C., 1977, Corvallis, Oregon, crustal and upper mantle structure from teleseismic P and S waves: Bull. Seism. Soc. Am., **67**, 713–724.

Payne, M., Eriksen, E., and Rape, T., 1994, Considerations for high-resolution VSP imaging: The Leading Edge, **3**, 173–179.

Pratt, R., 1999, Seismic waveform inversion in the frequency domain, Part 1: Theory and verification in a physical model: Geophysics, **64**, 888–901.

Prucha, M., Biondi, B., and Symes, W., 1999, Angle-domain common-image gathers by wave-equation migration: 69th Ann. Internat. Meeting, Soc. of Expl. Geophys., Expanded Abstracts, 824–827.

Rickett, J., and Sava, P., 2002, Offset and angle-domain common image-point gathers for shot profile migration: Geophysics, **67**, 883–889.

Rosales, D. A., and Biondi, B., 2005, Converted-mode angle-domain common-image gathers for migration velocity analysis: SEP–**120**, 283–296.

Rosales, D., and Rickett, J., 2001, *ps*-wave polarity reversal in angle domain common-image gathers: SEP–**108**, 35–44.

Sava, P., and Fomel, S., 2003a, Angle-domain common image gathers by wavefield continuation methods: Geophysics, **68**, no. 3, 1065–1074.

Sava, P., and Fomel, S., 2003b, Angle-domain common-image gathers by wavefield continuation methods: Geophysics, **68**, 1065–1074.

Sheley, D., and Schuster, G., 2003, Reduced-time migration of transmitted P-S waves: Geophysics, **68**, 1695–1707.

Shragge, J., Artman, B., and Wilson, C., 2005, Shot profile migration of teleseismic wavefields: Submitted to Geophysics.

Shragge, J., 2003, Phase-shift migration of approximate zero-offset teleseismic data: SEP–**113**, 145–156.

Sirgue, L., and Pratt, R., 2004, Efficient waveform inversion and imaging: A strategy for selecting temporal frequencies: Geophysics, **69**, 231–248.

Sullivan, C., Ross, A., J., L., Urban, D., Hornby, B., West, C., Garing, J., Paulsson, B., Karrenbach, M., and Milligan, P., 2003, A 3D massive VSP survey at Milne Point, Alaska: 73rd Ann. Internat. Mtg., Soc. of Expl. Geophys., Expanded Abstracts.

VanDecar, J., 1991, Upper-mantle structure of the Cascadia subduction zone from non-linear teleseismic travel-time inversion: Ph.D. thesis, 165 pp., Univ. of Wash., Seattle.